Journal of Medical Imaging

MedicalImaging.SPIEDigitalLibrary.org

Reconstruction of color biomedical images by means of quaternion generic Jacobi-Fourier moments in the framework of polar pixels

César Camacho-Bello
Alfonso Padilla-Vivanco
Carina Toxqui-Quitl
José Javier Báez-Rojas

SPIE.

César Camacho-Bello, Alfonso Padilla-Vivanco, Carina Toxqui-Quitl, José Javier Báez-Rojas, "Reconstruction of color biomedical images by means of quaternion generic Jacobi-Fourier moments in the framework of polar pixels," *J. Med. Imag.* **3**(1), 014004 (2016), doi: 10.1117/1.JMI.3.1.014004.

Reconstruction of color biomedical images by means of quaternion generic Jacobi-Fourier moments in the framework of polar pixels

César Camacho-Bello,[a,*] Alfonso Padilla-Vivanco,[a] Carina Toxqui-Quitl,[a] and José Javier Báez-Rojas[b]
[a]Universidad Politécnica de Tulancingo, Ingenierías No. 100, Hidalgo 43629, México
[b]Instituto Nacional de Astrofísica, Óptica y Electrónica. Luis Enrique Erro No. 1, Puebla 72840, México

Abstract. A detailed analysis of the quaternion generic Jacobi-Fourier moments (QGJFMs) for color image description is presented. In order to reach numerical stability, a recursive approach is used during the computation of the generic Jacobi radial polynomials. Moreover, a search criterion is performed to establish the best values for the parameters α and β of the radial Jacobi polynomial families. Additionally, a polar pixel approach is taken into account to increase the numerical accuracy in the calculation of the QGJFMs. To prove the mathematical theory, some color images from optical microscopy and human retina are used. Experiments and results about color image reconstruction are presented.
[DOI: 10.1117/1.JMI.3.1.014004]

Keywords: quaternion moments; Jacobi polynomial; color microscopy images; polar pixels; color image.

Paper 15141R received Jul. 9, 2015; accepted for publication Feb. 16, 2016; published online Mar. 11, 2016.

1 Introduction

In recent years, moments have been successfully used in a variety of research areas such as image registration,[1] face recognition,[2] angle estimation,[3] watermarking,[4] pattern reconstruction,[5] medical imaging,[6–8] focus measures,[9] image analysis,[10] forensic applications,[11] gait phase detection,[12] and so forth. In the 1960s, Hu[13] introduced a set of invariants based on the low-order geometric moments for pattern recognition tasks. Almost two decades later, Teague[14] proposed Zernike and Legendre moments derived from the basis set of orthogonal polynomials. It is known that one of the main advantages of moments with orthogonal basis functions is the ability to represent the global features of an image by a set of mutually independent descriptors, with a minimal amount of information redundancy. As stated by Bhatia and Wolf,[15] there are an infinite number of orthogonal sets inside the unit circle. Some orthogonal moments are derived from the basis set of pseudo-Zernike,[16] Chebyshev-Fourier,[17] orthogonal Fourier-Mellin,[18] radial harmonic Fourier,[19] and Bessel-Fourier[20] polynomials. Additionally, new orthogonal basis sets of circular moments have been proposed from the generic formula of the Jacobi radial polynomials,[21–23] where each set can be generated by combinations of two real parameters, which are commonly denoted as α and β. Also, Jacobi-Fourier moments (JFMs) have been successfully proven in pattern recognition,[24] image analysis,[25] and machine vision applications.[26] Recently, quaternion color moments have been introduced on the basis set of Fourier-Mellin,[27] Zernike,[28] and Bessel-Fourier polynomials.[29] These works have extended the capabilities of moments for describing color or *RGB* images. Consequently, new invariant descriptors have been proposed for pattern recognition while new algorithms for image reconstruction also have been studied. In the same direction, Karakasis et al.[30] presented a general framework for computing accurate quaternion color moments based on different orthogonal polynomials, from continuous to discrete polynomials and from Cartesian to circular symmetries.

On the other hand, in Ref. 23, there exists an analysis of the interconversion between the two historical definitions of the radial Jacobi polynomials; this interesting paper points out and clears the confusing points between both definitions. However, the computations of the polynomials through these formulas take into account the calculation of factorials of high orders. Unfortunately, this method of computing the radial polynomials causes strong numerical instability and inaccuracy for orders higher than $n = 21$. This effect is most evident in the reconstruction of large images as those acquired in the biomedical areas.

In many biomedical laboratories, it is a common task to count some microscopic specimens in order to help the clinical analysis or during the diagnostic of some diseases. A quality control program for clinical laboratories is commonly described by features such as accuracy, precision, tendency to avoid erroneous results, and tendency to avoid systematically different results in different laboratories. All of these situations should be supported by the use of automatic methods of pattern recognition and by the employment of digital image techniques, which must be based on numerical features increasingly more accurate and faster during the data processing.

In another context, retina images have been of interest in many scientific analyses as the biometric identification of people, among other applications. Due to this fact, new numerical approaches to analyze these kinds of images are continuously required. In this paper, we research the capabilities of image description from the quaternion generic Jacobi-Fourier moments (QGJFMs). This investigation makes use of the variations of the

*Address all correspondence to: César Camacho-Bello, E-mail: cesar.camacho@upt.edu.mx

2329-4302/2016/$25.00 © 2016 SPIE

Jacobi polynomials by the α and β parameters, because they can use different sets of quaternion orthogonal moments such as quaternion orthogonal Fourier-Mellin moments ($\alpha = 2, \beta = 2$), quaternion Chebyshev-Fourier moments ($\alpha = 2, \beta = 3/2$), quaternion pseudo Jacobi-Fourier moments ($\alpha = 4,\ \beta = 3$), quaternion Legendre-Fourier moments ($\alpha = 1,\ \beta = 1$), quaternion pseudo-Zernike moments, and quaternion Zernike moments. The analysis is done in the context of a polar pixel scheme and by means of an algorithm for fast computation and high precision.[25,26] Furthermore, this study proposes the search for optimal parameters α and β of QGJFMs to significantly improve the quality of reconstruction. The analysis is then applied to reconstruct some color biomedical images in circular symmetry as validation tests of the algorithm.

This work is organized as follows. Section 2 introduces QGJFMs. In Sec. 3, the QGJFMs are computed on the geometry of polar pixels and presents an image conversion via bicubic interpolation for the high-precision computing of QGJFMs. In Sec. 4, an inverse quaternion transformation for reconstruction of RGB images is presented. Also, in this section, the normalized image reconstruction error is used as a measurement of image reconstruction. Section 5 takes into account a numerical comparison with other methods in the context of a test RGB image for different orders of reconstruction. Some experimental results are presented in Sec. 6, where an evaluation of accurate and fast computation through some color biomedical images has been used. Finally, the conclusions of this research are presented in Sec. 7.

2 Quaternion Generic Jacobi-Fourier Moments

Recently, quaternion moments have been used as a novel method for describing color images. The quaternion theory is a generalization of the complex theory of numbers. A quaternion q is composed of one real part and three imaginary parts; it takes the following form:

$$q = a + b\mathbf{i} + c\mathbf{j} + d\mathbf{k}, \tag{1}$$

where a, b, c, and d are real numbers and $\mathbf{i}$, $\mathbf{j}$, and $\mathbf{k}$ are three imaginary units. The basic operations among them are in accord with the following rules:

$$\begin{aligned} \mathbf{i}^2 &= \mathbf{j}^2 = \mathbf{k}^2 = -1, \\ \mathbf{ij} &= -\mathbf{ji} = \mathbf{k}, \\ \mathbf{jk} &= -\mathbf{kj} = \mathbf{i}, \\ \mathbf{ki} &= -\mathbf{ik} = \mathbf{j}. \end{aligned} \tag{2}$$

The conjugate and modulus of a quaternion are, respectively, defined by

$$q^* = a - b\mathbf{i} - c\mathbf{j} - d\mathbf{k}, \tag{3}$$

$$|q| = \sqrt{a^2 + b^2 + c^2 + d^2}. \tag{4}$$

Using the quaternion representation, an RGB image $f(r,\theta)$ defined in polar coordinates can be considered as a quaternion-based model for color images, which is given as follows:

$$f(r,\theta) = f_R(r,\theta)\mathbf{i} + f_G(r,\theta)\mathbf{j} + f_B(r,\theta)\mathbf{k}, \tag{5}$$

where the functions $f_R(r,\theta)$, $f_G(r,\theta)$, and $f_B(r,\theta)$ are, respectively, the red, green, and blue channels of the image.

According to the noncommutative property of quaternion multiplication, there are two types of QGJFMs of order n and repetition m, namely, the right-side moments defined by

$$\phi_{n,m}^{\text{right}} = \int_0^{2\pi}\int_0^1 f(r,\theta) J_n(\alpha,\beta,r)\exp(\mu m\theta) r\,\mathrm{d}r\,\mathrm{d}\theta, \tag{6}$$

and the left-side moments, which are given as follows:

$$\phi_{n,m}^{\text{left}} = \int_0^{2\pi}\int_0^1 \exp(\mu m\theta) f(r,\theta) J_n(\alpha,\beta,r) r\,\mathrm{d}r\,\mathrm{d}\theta, \tag{7}$$

where $J_n(\alpha,\beta,r)$ are the generic Jacobi radial polynomials.[23] The real numbers α and β define a specific radial polynomial family and μ is a unit pure quaternion. It can be used as $\mu = (\mathbf{i}+\mathbf{j}+\mathbf{k})/\sqrt{3}$. Due to the anti-involution property of quaternion conjugation, the left-side and right-side transforms have the following relationship:

$$\phi_{n,m}^{\text{left}} = -\phi_{n,-m}^{\text{right}}. \tag{8}$$

For the case of discrete image functions, Eqs. (6) and (7) cannot be directly applied. The integrals of these equations have to be replaced by summations and the discrete image function has to be normalized inside the unit disk; this approach is known as the zeroth-order approximation or direct method. This procedure is briefly described below.

Let $f(r_{i,j},\theta_{i,j})$ be a discrete image function with spatial dimensions $M \times N$. Its right discrete quaternion moments $\phi_{n,m}^{\text{right}}$ are given by

$$\phi_{n,m}^{\text{right}} = \sum_{i=0}^{M-1}\sum_{j=0}^{N-1} f(r_{i,j},\theta_{i,j}) J_n(\alpha,\beta,r_{i,j})\exp(\mu m\theta_{i,j}), \tag{9}$$

where the discrete polar coordinates are expressed by

$$r_{i,j} = \sqrt{x_i^2 + y_j^2}, \qquad r_{i,j} \le 1, \tag{10}$$

$$\theta_{i,j} = \arctan\left(\frac{y_j}{x_i}\right), \tag{11}$$

and they are transformed as follows:

$$x_i = -1 + \frac{2i}{N-1}, \qquad y_j = -1 + \frac{2j}{M-1}, \tag{12}$$

where $i = 0,\ldots,N-1$ and $j = 0,\ldots,M-1$.

3 Computation of the Quaternion Generic Jacobi-Fourier Moments in Polar Pixels

In a previous analysis,[31] it has been demonstrated that two types of errors occur in the direct calculation method of orthogonal moments, namely, geometric error and numerical integration error. To increase the numerical accuracy calculation, Xin et al.[32] proposed an algorithm based on changing the shape of the square pixels for a polar pixels scheme. Recently, Camacho-Bello et al.[25] proposed a recurrence relation to eliminate the numerical instability of the orthogonal polynomials and to compare with other methods in terms of invariance, reconstruction error, and computation time. In terms of our

research in this section, a recurrence relationship for computing the generic radial Jacobi polynomials will be used.[26]

3.1 *Recurrence Relation of Jacobi Polynomials*

The recurrence relation with respect to n is used to increase the numerical stability for the computation of the shifted radial Jacobi polynomials. The recursive relationship is given by

$$A_n J_n(\alpha,\beta,r) = (2r - 1 - B_n)J_{n-1}(\alpha,\beta,r) - A_{n-1}J_{n-2}(\alpha,\beta,r), \tag{13}$$

where $r \in [0,1]$, $\alpha - \beta > -1$, β, $\alpha > 0$, and the coefficients A_n and B_n are computed as follows:

$$A_n = \sqrt{\frac{4n(n+\alpha-\beta)(n+\beta-1)(n+\alpha-1)}{(2n+\alpha-1)^2(2n+\alpha)(2n+\alpha-2)}}, \tag{14}$$

$$B_n = \frac{(\alpha-1)(2\beta-\alpha-1)}{(2n+\alpha-1)[2(n-1)+\alpha-1]}. \tag{15}$$

To start with the numerical computation, the Jacobi polynomials of zero and first normalized orders are given by

$$J_0(\alpha,\beta,r) = \sqrt{\frac{w(\alpha,\beta,r)}{b_0(\alpha,\beta)}}, \tag{16}$$

$$J_1(\alpha,\beta,r) = J_0(\alpha,\beta,r)\sqrt{\frac{(\alpha+2)\beta}{\alpha-\beta+1}}\left(\frac{\alpha+1}{\beta}r - 1\right). \tag{17}$$

The advantage of the recurrence relationships is that they can diminish the computation time of the radial polynomials because the calculation of factorials is not taken into account. Moreover, using the recurrence relation, the computation accuracy of the n'th power of r ($n > 21$) is increased.

3.2 *Proposed Scheme of Polar Pixels for Quaternion Generic Jacobi-Fourier Moments*

The unit disk of polar pixels scheme is uniformly divided along the radial direction into U sections, with radial distance of $r_u = u/U$, where $u = 1 \ldots U$. The number of polar pixels in the u'th ring is $S_u = (2u-1)V$, with angles $\theta_{uv} = (v-1)2\pi/S_u$, where $v = 1 \ldots S_u$ and V is the number of sectors contained in the innermost section. In practice, Xin et al.[32] recommended to set the value of $V = 4$ and $N/2 \le U \le N$ for an $N \times N$ image. Figure 1 shows the polar pixels scheme with $V = 4$ and $U = 5$. The calculation of the QGJFMs in the framework of polar pixels is performed by the summation of all sectors inside the unit disk. For this calculation, Eq. (9) can be rewritten as

$$\hat{\phi}_{n,m}^{\text{right}} = \sum_{u=1}^{U}\sum_{v=1}^{(2u-1)V} \hat{f}(r_{uv},\theta_{uv})\omega_{nm}(r_{uv},\theta_{uv}), \tag{18}$$

where $\hat{f}(r_{uv},\theta_{uv})$ is an approximation of the function $f(r_{i,j},\theta_{i,j})$ defined over a set of concentric sectors Ω_{uv}, and the factor $\omega_{nm}(r_{uv},\theta_{uv})$ is given by

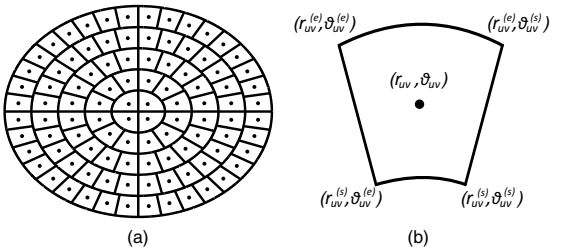

Fig. 1 (a) Polar pixel representation of an image and (b) polar pixel sector Ω_{uv}.

$$\omega_{nm}(r_{uv},\theta_{uv}) = \iint_{\Omega_{uv}} J_n(\alpha,\beta,r)\exp(\mu m\theta)r\mathrm{d}r\,\mathrm{d}\theta. \tag{19}$$

The integrals of Eq. (19) can be separated as

$$\omega_{nm}(r_{uv},\theta_{uv}) = \int_{r_{uv}^{(s)}}^{r_{uv}^{(e)}} J_n(\alpha,\beta,r)r\mathrm{d}r \int_{\theta_{uv}^{(s)}}^{\theta_{uv}^{(e)}} \exp(\mu m\theta)\mathrm{d}\theta, \tag{20}$$

where $r_{uv}^{(s)}$ and $r_{uv}^{(e)}$ denote, respectively, the starting and ending radii of the sector Ω_{uv}, while $\theta_{uv}^{(s)}$ and $\theta_{uv}^{(e)}$ denote the starting and ending angles of the sector. A scheme of a polar pixel is shown in Fig. 1(b). Using the Euler formula for quaternions, Eq. (20) can be seen as follows:

$$\omega_{nm}(r_{uv},\theta_{uv}) = \left[\int_{r_{uv}^{(s)}}^{r_{uv}^{(e)}} J_n(\alpha,\beta,r)r\mathrm{d}r\right] \times \left[\int_{\theta_{uv}^{(s)}}^{\theta_{uv}^{(e)}} \cos(m\theta)\mathrm{d}\theta + \mu\int_{\theta_{uv}^{(s)}}^{\theta_{uv}^{(e)}} \sin(m\theta)\mathrm{d}\theta\right]. \tag{21}$$

Rewriting Eq. (21) in the next form produces

$$\omega_{nm}(r_{uv},\theta_{uv}) = I_{uv}^{J_n} \times [I_{uv}^{\cos} + \mu I_{uv}^{\sin}]. \tag{22}$$

It is evident from Eq. (22) that three integrals can be obtained, which can be expressed as

$$I_{uv}^{J_n} = \int_{r_{uv}^{(s)}}^{r_{uv}^{(e)}} J_n(\alpha,\beta,r)r\mathrm{d}r, \tag{23}$$

$$I_{uv}^{\cos} = \int_{\theta_{uv}^{(s)}}^{\theta_{uv}^{(e)}} \cos(m\theta)\mathrm{d}\theta, \tag{24}$$

$$I_{uv}^{\sin} = \int_{\theta_{uv}^{(s)}}^{\theta_{uv}^{(e)}} \sin(m\theta)\mathrm{d}\theta. \tag{25}$$

In order to solve the integral of Eq. (23), Camacho-Bello et al.[25] proposed to use a 10-point Gaussian quadrature rule, along with the recurrence relationship with respect to the order n for computing the generic radial Jacobi polynomials.

Typically, the aforementioned procedure is less accurate than the direct method, but is numerically more stable for orders greater than 21. Thus, the composite Gaussian quadrature rule for numerical integration of the generic Jacobi radial polynomials can be stated as

$$I_{uv}^{J_n} = \frac{r_{uv}^{(e)} - r_{uv}^{(s)}}{2} \sum_{k=1}^{10} \eta_k J_n \left[\alpha, \beta, \frac{r_{uv}^{(e)} - r_{uv}^{(s)}}{2} z_k + \frac{r_{uv}^{(e)} + r_{uv}^{(s)}}{2} \right], \tag{26}$$

where η_k are weights and $z_k \in [-1,1]$ are the points where the function is evaluated. The values for η_k and z_k are given in Table 1.

The integrals of Eqs. (24) and (25) can be analytically calculated as follows:

$$I_{uv}^{\cos} = \begin{cases} \frac{1}{jm}[\sin(jm\theta_{uv}^{(e)}) - \sin(jm\theta_{uv}^{(s)})], & m \neq 0 \\ \theta_{uv}^{(e)} - \theta_{uv}^{(s)}, & m = 0 \end{cases} \tag{27}$$

$$I_{uv}^{\sin} = \frac{1}{jm}[\cos(jm\theta_{uv}^{(s)}) - \cos(jm\theta_{uv}^{(e)})]. \tag{28}$$

3.3 *Proposed Computation of Quaternion Generic Jacobi-Fourier Moments*

For the calculation of QGJFMs from the right-side transformation in a scheme of polar pixels, we have to represent $\hat{f}_R$, $\hat{f}_G$, and $\hat{f}_B$ as the components of an RGB image. These images can be transformed to a scheme of polar pixels.[20,25,26] Therefore, $f(r,\theta)$ from Eq. (5) can be replaced as

$$\hat{f}(r,\theta) = \hat{f}_R(r,\theta)\mathbf{i} + \hat{f}_G(r,\theta)\mathbf{j} + \hat{f}_B(r,\theta)\mathbf{k}. \tag{29}$$

Substituting Eq. (29) into Eq. (6) leads to

$$\hat{\phi}_{n,m}^{\text{right}} = \sum_{u=1}^{U} \sum_{v=1}^{(2u-1)V} [\hat{f}_R(r,\theta)\mathbf{i} + \hat{f}_G(r,\theta)\mathbf{j} + \hat{f}_B(r,\theta)\mathbf{k}] \times \omega_{nm}(r_{uv},\theta_{uv}). \tag{30}$$

Using the basic rules of Eq. (2), we can express the QGJFMs as

Table 1 Weights (η_k) and location of sampling points (z_k) for 10-point Gaussian quadrature.

k	η_k	z_k
1	0.0666713443	−0.9739065285
2	0.1494513492	−0.8650633667
3	0.2190863625	−0.6794095683
4	0.2692667193	−0.4333953941
5	0.2955242247	−0.1488743390
6	0.2955242247	0.1488743390
7	0.2692667193	0.4333953941
8	0.2190863625	0.6794095683
9	0.1494513492	0.8650633667
10	0.0666713443	0.9739065285

$$\begin{aligned} \hat{\phi}_{n,m}^{\text{right}} = {} & \mathbf{i} \sum_{u=1}^{U} \sum_{v=1}^{(2u-1)V} \hat{f}_R(r_{uv},\theta_{uv}) \omega_{nm}(r_{uv},\theta_{uv}) \\ & + \mathbf{j} \sum_{u=1}^{U} \sum_{v=1}^{(2u-1)V} \hat{f}_G(r_{uv},\theta_{uv}) \omega_{nm}(r_{uv},\theta_{uv}) \\ & + \mathbf{k} \sum_{u=1}^{U} \sum_{v=1}^{(2u-1)V} \hat{f}_B(r_{uv},\theta_{uv}) \omega_{nm}(r_{uv},\theta_{uv}). \end{aligned} \tag{31}$$

As stated earlier, $\omega_{n,m}$ can be represented by Eq. (22), and by virtue of this relation, Eq. (31) takes the following form:

$$\begin{aligned} \hat{\phi}_{n,m}^{\text{right}} = {} & \mathbf{i} \sum_{u=1}^{U} \sum_{v=1}^{(2u-1)V} \hat{f}_R(r_{uv},\theta_{uv}) I_{uv}[I_{uv}^{\cos} + \mu I_{uv}^{\sin}] \\ & + \mathbf{j} \sum_{u=1}^{U} \sum_{v=1}^{(2u-1)V} \hat{f}_G(r_{uv},\theta_{uv}) I_{uv}[I_{uv}^{\cos} + \mu I_{uv}^{\sin}] \\ & + \mathbf{k} \sum_{u=1}^{U} \sum_{v=1}^{(2u-1)V} \hat{f}_B(r_{uv},\theta_{uv}) I_{uv}[I_{uv}^{\cos} + \mu I_{uv}^{\sin}]. \end{aligned} \tag{32}$$

At this point, we can again use the basic rules for quaternions defined in Eq. (2). Then, distributing the integrals for both sine and cosine, Eq. (32) can be written as follows:

$$\begin{aligned} \hat{\phi}_{n,m}^{\text{right}} = {} & \mathbf{i} \left[\sum_{u=1}^{U} \sum_{v=1}^{(2u-1)V} \hat{f}_R(r_{uv},\theta_{uv}) I_{uv} I_{uv}^{\cos} + \mu \sum_{u=1}^{U} \sum_{v=1}^{(2u-1)V} \hat{f}_R(r_{uv},\theta_{uv}) I_{uv} I_{uv}^{\sin} \right] \\ & + \mathbf{j} \left[\sum_{u=1}^{U} \sum_{v=1}^{(2u-1)V} \hat{f}_G(r_{uv},\theta_{uv}) I_{uv} I_{uv}^{\cos} + \mu \sum_{u=1}^{U} \sum_{v=1}^{(2u-1)V} \hat{f}_G(r_{uv},\theta_{uv}) I_{uv} I_{uv}^{\sin} \right] \\ & \mathbf{k} \left[\sum_{u=1}^{U} \sum_{v=1}^{(2u-1)V} \hat{f}_B(r_{uv},\theta_{uv}) I_{uv} I_{uv}^{\cos} + \mu \sum_{u=1}^{U} \sum_{v=1}^{(2u-1)V} \hat{f}_B(r_{uv},\theta_{uv}) I_{uv} I_{uv}^{\sin} \right]. \end{aligned} \tag{33}$$

Taking into account the proposed value for the quaternion μ, the QGJFMs of an *RGB* image in polar pixels are expressed by

$$\begin{aligned} \hat{\phi}_{n,m}^{\text{right}} = {} & \mathbf{i} \left\{ \text{Re}[\hat{\phi}_{nm}(\hat{f}_R)] + \frac{(\mathbf{i}+\mathbf{j}+\mathbf{k})}{\sqrt{3}} \text{Im}[\hat{\phi}_{nm}(\hat{f}_R)] \right\} \\ & + \mathbf{j} \left\{ \text{Re}[\hat{\phi}_{nm}(\hat{f}_G)] + \frac{(\mathbf{i}+\mathbf{j}+\mathbf{k})}{\sqrt{3}} \text{Im}[\hat{\phi}_{nm}(\hat{f}_G)] \right\} \\ & + \mathbf{k} \left\{ \text{Re}[\hat{\phi}_{nm}(\hat{f}_B)] + \frac{(\mathbf{i}+\mathbf{j}+\mathbf{k})}{\sqrt{3}} \text{Im}[\hat{\phi}_{nm}(\hat{f}_B)] \right\}. \end{aligned} \tag{34}$$

Finally,

$$\hat{\phi}_{n,m}^{\text{right}} = A_{n,m}^{\text{right}} + \mathbf{i}B_{n,m}^{\text{right}} + \mathbf{j}C_{n,m}^{\text{right}} + \mathbf{k}D_{n,m}^{\text{right}}, \tag{35}$$

where

$$A_{n,m}^{\text{right}} = -\frac{1}{\sqrt{3}}\{\text{Im}[\hat{\phi}_{nm}(\hat{f}_R)] + \text{Im}[\hat{\phi}_{nm}(\hat{f}_G)] + \text{Im}[\hat{\phi}_{nm}(\hat{f}_B)]\},$$
$$B_{n,m}^{\text{right}} = \text{Re}[\hat{\phi}_{nm}(\hat{f}_R)] + \frac{1}{\sqrt{3}}\{\text{Im}[\hat{\phi}_{nm}(\hat{f}_G)] - \text{Im}[\hat{\phi}_{nm}(\hat{f}_B)]\},$$
$$C_{n,m}^{\text{right}} = \text{Re}[\hat{\phi}_{nm}(\hat{f}_G)] + \frac{1}{\sqrt{3}}\{\text{Im}[\hat{\phi}_{nm}(\hat{f}_B)] - \text{Im}[\hat{\phi}_{nm}(\hat{f}_R)]\},$$
$$D_{n,m}^{\text{right}} = \text{Re}[\hat{\phi}_{nm}(\hat{f}_B)] + \frac{1}{\sqrt{3}}\{\text{Im}[\hat{\phi}_{nm}(\hat{f}_R)] - \text{Im}[\hat{\phi}_{nm}(\hat{f}_G)]\}. \tag{36}$$

4 RGB Image Reconstruction

The capacity of description of the QGJFMs is done by means of its inverse transformation. According to the inverse quaternion Jacobi-Fourier transform, an original RGB image $f(r,\theta)$ can be reconstructed by a finite number of QGJFMs, which is given by

$$\tilde{f}(r,\theta) = \tilde{f}_A(r,\theta) + \tilde{f}_B(r,\theta)\mathbf{i} + \tilde{f}_C(r,\theta)\mathbf{j} + \tilde{f}_D(r,\theta)\mathbf{k}, \tag{37}$$

where

$$\tilde{f}_A(r,\theta) = \text{Re}[\tilde{A}(r,\theta)] - \frac{1}{\sqrt{3}}\{\text{Im}[\tilde{B}(r,\theta)] + \text{Im}[\tilde{C}(r,\theta)] + \text{Im}[\tilde{D}(r,\theta)]\},$$
$$\tilde{f}_B(r,\theta) = \text{Re}[\tilde{B}(r,\theta)] + \frac{1}{\sqrt{3}}\{\text{Im}[\tilde{A}(r,\theta)] + \text{Im}[\tilde{C}(r,\theta)] - \text{Im}[\tilde{D}(r,\theta)]\},$$
$$\tilde{f}_C(r,\theta) = \text{Re}[\tilde{C}(r,\theta)] + \frac{1}{\sqrt{3}}\{\text{Im}[\tilde{A}(r,\theta)] - \text{Im}[\tilde{B}(r,\theta)] + \text{Im}[\tilde{D}(r,\theta)]\},$$
$$\tilde{f}_D(r,\theta) = \text{Re}[\tilde{D}(r,\theta)] + \frac{1}{\sqrt{3}}\{\text{Im}[\tilde{A}(r,\theta)] + \text{Im}[\tilde{B}(r,\theta)] - \text{Im}[\tilde{C}(r,\theta)]\}, \tag{38}$$

$$\tilde{A}(r_{i,j},\theta_{i,j}) = \sum_{n=0}^{L}\sum_{m=0}^{L} A_{n,m}^{\text{right}} J_n(\alpha,\beta,r_{i,j})\exp(jm\theta_{i,j}),$$
$$\tilde{B}(r_{i,j},\theta_{i,j}) = \sum_{n=0}^{L}\sum_{m=0}^{L} B_{n,m}^{\text{right}} J_n(\alpha,\beta,r_{i,j})\exp(jm\theta_{i,j}),$$
$$\tilde{C}(r_{i,j},\theta_{i,j}) = \sum_{n=0}^{L}\sum_{m=0}^{L} C_{n,m}^{\text{right}} J_n(\alpha,\beta,r_{i,j})\exp(jm\theta_{i,j}),$$
$$\tilde{D}(r_{i,j},\theta_{i,j}) = \sum_{n=0}^{L}\sum_{m=0}^{L} D_{n,m}^{\text{right}} J_n(\alpha,\beta,r_{i,j})\exp(jm\theta_{i,j}). \tag{39}$$

Note that $\tilde{f}_B(r,\theta)$, $\tilde{f}_C(r,\theta)$, and $\tilde{f}_D(r,\theta)$ represent the red, green, and blue components of the reconstructed color image, respectively, and L is the maximum order of QGJFMs used in the reconstruction. Typically, the reconstruction formula has been used to recover the image information up to a certain level of approximation.

4.1 *RGB Image Reconstruction Error*

In this section, a reconstruction metric based on the normalized image reconstruction error (NIRE) is presented. It is defined as the normalized square error between the input image $f_c(x,y)$ and its reconstruction $\tilde{f}_c(x,y)$. This error is presented in discrete form for each channel c of the RGB image, and it is given by

$$\text{NIRE}_c = \frac{\sum_{y=1}^{N}\sum_{x=1}^{M}[f_c(x,y) - \tilde{f}_c(x,y)]^2}{\sum_{y=1}^{N}\sum_{x=1}^{M} f_c^2(x,y)}. \tag{40}$$

The measure for the reconstruction error of a color image that considers the three channels is given by

$$\text{MeanNIRE} = \frac{\text{NIRE}_R + \text{NIRE}_G + \text{NIRE}_B}{3}. \tag{41}$$

Also, we have assumed that the image sizes are $M \times N$.

5 Comparison with Other Methods

The zero-order approximation is commonly used because of its easy implementation. However, it requires replacing the double integral by a double sum. Typically, this approximation during the computation of the quaternion moments creates a poor reconstruction in RGB images. For this reason, Karakasis et al.[30] proposed an alternative numerical approximation that uses some recurrence relations in order to improve the performance calculation. In this section, we compare the approach of polar pixels with zero-order approximation and the numerical approximation in terms of image reconstruction, reconstruction error, and computation time. As in Ref. 30, we use the standard image Lena with the quaternion orthogonal Fourier-Mellin moments ($\alpha = \beta = 2$). Figures 2 and 3 show the Lena image reconstruction and the NIRE, respectively.

Since the computation time does not depend on image content, only one image is considered for the analysis. The code is implemented using MATLAB® with a Sony Electronics Inc. Model VAIO R Computer Notebook PC with Intel Core™i5-2430M CPU 2.40 GHz processor with 4 GB of RAM. Figure 4 shows the computation time of the different methods. The zero-order approximation calculation has better times. However, the scheme of polar pixels has reasonable computing times with minimal reconstruction error.

6 Experimental Results

In this section, we present the reconstruction results obtained using some color test images from optical microscopy and the human retina. These RGB test images are shown in Fig. 5. Using Eq. (38), we have reconstructed the three cases of test images. The results are shown in Figs. 6(a), 6(b), and 6(c).The results for the NIRE from the RGB test images are shown in Figs. 6(d), 6(e), and 6(f). To obtain these results, we have considered image sizes of 512×512 pixels and $\alpha = \beta = 1, 2, 3, 4, 5$.

6.1 *Searching of α and β Parameters*

As mentioned in Sec. 1, Bhatia and Wolf[15] pointed out that there is an infinite number of complete sets of orthogonal polynomials, which are invariant to rotation and can be obtained from the generic Jacobi polynomial formula. Each set is obtained by the combination of the parameters α and β. Therefore, a set of orthogonal moments could be chosen to fit specific applications. We define the mean of Mean_NIRE as metric to quantitatively

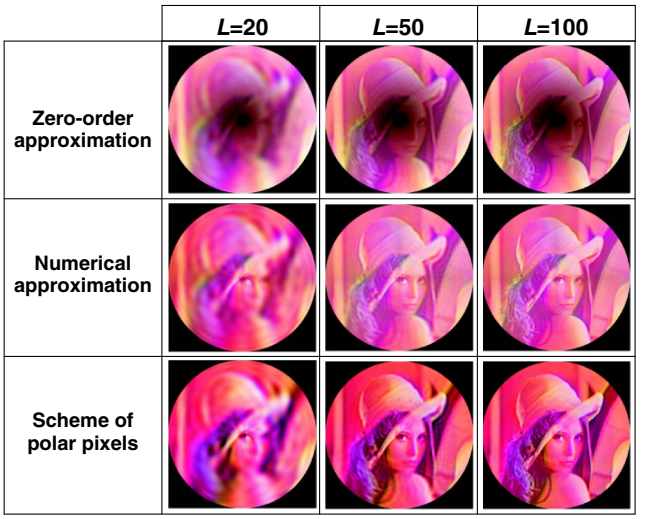

Fig. 2 Lena image reconstruction of 512×512 pixels with different methods for $L = 20, 50, 100$.

evaluate the best combinations of α and β. The mean value of Mean_NIRE is given by

$$\Psi(\alpha, \beta, p) = \frac{1}{p} \sum_{L=1}^{p} \text{MeanNIRE}(L, \alpha, \beta), \tag{42}$$

where L is the maximum order of QGJFMs used in the reconstruction of the input image and p is the cutting order. The cutting order p can find the optimal parameters for moments of low and high orders. In general, low-order moments represent the global shape of an image, and high-order moments the detail.[5] The search space is restricted by $\alpha - \beta > -1$ and the sections with minimum values represent the neighborhood of the best combinations of α and β. Figures 6(g), 6(h), and 6(i) show the exhaustive searches performed for the RGB test images with values of $\alpha = 1...10$ and $\beta = 1...10$.

In general, image reconstruction has been commonly used to describe how well an image can be retrieved by a small set of its moments. Here, the interest is to discuss the results obtained in each test case.

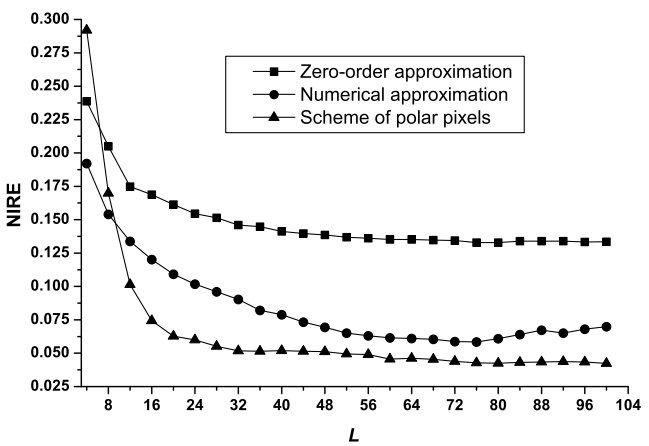

Fig. 3 NIRE of Lena image with size 512×512 pixels for different computation methods.

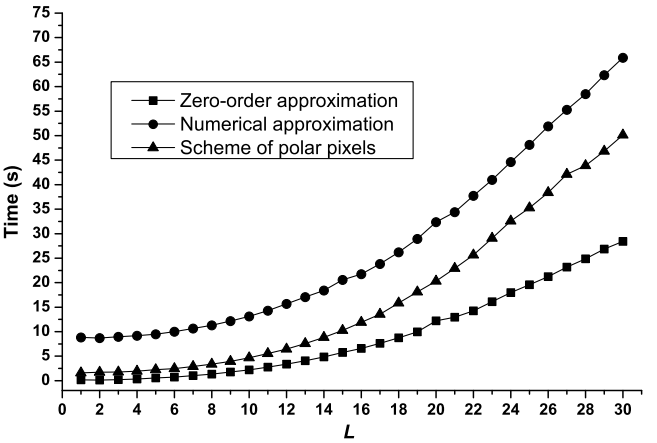

Fig. 4 Computation time of Lena image with size 512×512 pixels for different computation methods.

6.1.1 *Yogurt bacteria image*

As is shown in Fig. 6(g), the best values of the search are located when $\alpha = \beta$. According to its NIRE graph of Fig. 6(d), the tendency of error is to go down as the order L is increased. Moreover, the RGB image is completely reconstructed before the order $L = 90$. Figure 6(a) shows the RGB image reconstruction when $\alpha = \beta = 1$, which is the best value found in the search of Fig. 6(g). It is clear that the reconstruction is not severely affected by the Gaussian noise acquired during the registration of the input image.

6.1.2 *Human retina image*

In this case, the search for the minimum values for the average of the NIRE yields $\alpha = \beta$. The NIRE graph of the best values found shown in Fig. 6(e) presents numerical oscillations and the tendency of error after the order $L = 60$ to increase. This behavior is explained by the low contrast presented in the input image of Fig. 5(b). As in the previous case, the best value in the search of Fig. 6(h) is found when $\alpha = \beta = 1$; the *RGB* image reconstruction results are shown in Fig. 6(b). In spite of these results, QGJFMs are capable of recovering the global information of the image including some high frequencies.

6.1.3 *Diatom image*

In the third case, the best results of the search neighborhood are when $\alpha = \beta$. Moreover, the *RGB* image reconstruction and

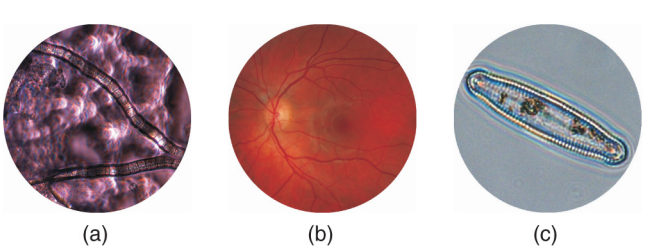

Fig. 5 RGB test images from (a) yogurt bacteria, (b) human retina, and (c) diatom. Yogurt bacteria and diatom are acquired using a microscope in bright field illumination. In the case of the diatom, a 100× microscope objective has been used in oil immersion.

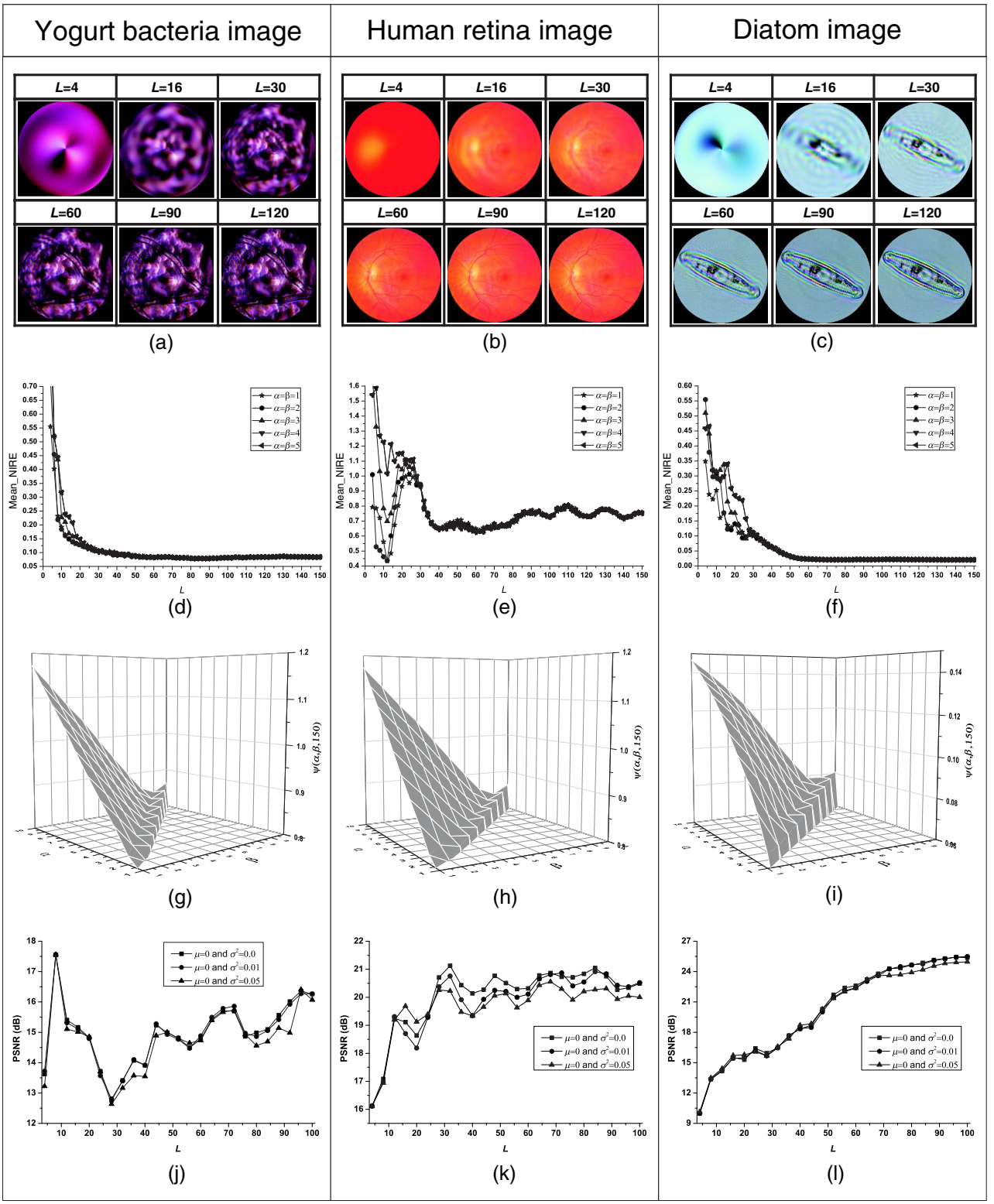

Fig. 6 Results of the test images: (a), (b), and (c) RGB image reconstruction, (d), (e), and (f) RGB image reconstruction error, (g), (h), and (i) searching of α and β parameters, and (j), (k), and (l) mean of PSNR.

NIRE with α and β best parameters present qualitatively and quantitatively good results, respectively. As shown in Fig. 6(f), NIRE decreases as L increases, reaching zero at $L = 150$. Unlike the prior case, the diatom image has a clear background and the object of interest is clearly identified. Finally, the RGB image reconstruction shown in Fig. 6(c) has $\alpha = \beta = 1$, which are the best parameters found in Fig. 6(i).

For all RGB test images, the best results are found when $\alpha = \beta$, especially when $\alpha = \beta = 1$, which would be the case of the quaternion Legendre-Fourier moments.

6.2 *Noisy Image Sensitivity*

Sensitivity to noise is a critical issue for quaternion moments. We compare the best parameters of QGJFMs ($\alpha = \beta = 1$) for peak signal-to-noise ratio (PSNR) and their performance for image reconstruction in the presence of noise, which is the ratio between a signal maximum power and the power of the signal noise, expressed in decibels. The PSNR for each channel c of the *RGB* image is given by

$$\mathrm{PSNR}_c = 10\log_{10}(255^2/\mathrm{MSE}_c), \tag{43}$$

where the mean square error (MSE_c) is defined as

$$\mathrm{MSE}_c = \frac{1}{N \times M}\sum_{i=0}^{N-1}\sum_{j=0}^{M-1}[f_c(i,j) - \tilde{f}_c(i,j)]^2. \tag{44}$$

The measure for the PSNR of an RGB image that considers the three channels is given by

$$\mathrm{MeanPSNR} = \frac{\mathrm{PSNR}_R + \mathrm{PSNR}_G + \mathrm{PSNR}_B}{3}. \tag{45}$$

Figures 6(j), 6(k), and 6(l) show the Mean_PSNR result from the *RGB* test images corrupted by an additive Gaussian noise. The results of the graphs show that the QGJFMs when $\alpha = \beta = 1$ remain unchanged for values $L < 15$, i.e., are resistant to Gaussian noise for quaternion moments of low order.

7 Conclusions

We have introduced QGJFMs for color image description in the scheme of polar pixels. We have proven a reconstruction algorithm for measuring the capacity of the QGJFMs in retrieving the features of some test RGB images. Also, we have a approach for high precision and fast computation of QGJFMs compared to other methods. Furthermore, the arrangement of polar pixels and the recurrence relationship used for different polynomial families improves the computation time and the reconstruction error in the case of *RGB* frames with large sizes.

The three test images used here present interesting characteristics. In the yogurt bacteria image, the background and object of interest are near the original colors. However, the QGJFMs have been able to recover all the information. In the case of the human retina image, new QGJFMs have obtained global information and the main high frequencies. Finally, for the diatom image, the background is strongly different from the specimen; this fact helps to practically recover all the RGB image. In general, these results have been found using the α and β parameters through the searching spaces for each particular case.

Acknowledgments

C. Camacho-Bello thanks CONACyT for the scholarship with number 423493.

References

1. B. Zitova and J. Flusser, "Image registration methods: a survey," *Image Vis. Comput.* **21**(11), 977–1000 (2003).
2. S. Farokhi et al., "Rotation and noise invariant near-infrared face recognition by means of Zernike moments and spectral regression discriminant analysis," *J. Electron. Imaging* **22**(1), 013030 (2013).
3. C. Camacho-Bello and J. Baez-Rojas, "Angle estimation using Hahn moments for image analysis," *Lec. Notes Comput. Sci.* **8827**, 127–134 (2014).
4. C. Singh and S. K. Ranade, "Rotation invariant moments and transforms for geometrically invariant image watermarking," *J. Electron. Imaging* **22**(1), 013034 (2013).
5. A. Padilla-Vivanco et al., "Comparative analysis of pattern reconstruction using orthogonal moments," *Opt. Eng.* **46**(1), 017002 (2007).
6. W. Liyun et al., "Spermatogonium image recognition using Zernike moments," *Comput. Methods Programs Biomed.* **95**(1), 10–22 (2009).
7. J. F. Mangin et al., "Brain morphometry using 3D moment invariants," *Med. Image Anal.* **8**(3), 187–196 (2004).
8. Z. Iscan, H. Dokur, and T. lmez, "Tumor detection by using Zernike moments on segmented magnetic resonance brain images," *Expert Syst. Appl.* **37**(3), 2540–2549 (2010).
9. E. Maalouf, B. Colicchio, and A. Dieterlen, "Fluorescence microscopy three-dimensional depth variant point spread function interpolation using Zernike moments," *J. Opt. Soc. Am. A* **28**(9), 1864–1870 (2011).
10. G. Papakostas, "*Moments and Moment Invariants: Theory and Applications*," Science Gate Publishing, Xhanti, Greece (2014).
11. G. AlGarni and M. Hamiane, "A novel technique for automatic shoe print image retrieval," *Forensic Sci. Int.* **181**(1), 10–14 (2008).
12. C. Camacho-Bello and J. Baez-Rojas, "Krawtchouk moments for gait phase detection," *Lec. Notes Comput. Sci.* **8827**, 787–793 (2014).
13. M. K. Hu, "Visual pattern recognition by moment invariants," *IRE Trans. Inf. Theory* **8**(2), 179–187 (1962).
14. M. R. Teague, "Image analysis via the general theory of moments," *J. Opt. Soc. Am.* **70**(8), 920–930 (1980).
15. A. B. Bhatia and E. Wolf, "On circular polynomials of Zernike and related orthogonal sets," *Math. Proc. Cambridge Philos. Soc.* **50**(1), 40–48 (1954).
16. G. Amu et al., "Image analysis by pseudo-Jacobi ($p = 4$, $q = 3$)-Fourier moments," *Appl. Opt.* **43**(10), 2093–2101 (2004).
17. Z. L. Ping, R. G. Wu, and Y. L. Sheng, "Image description with Chebyshev-Fourier moments," *J. Opt. Soc. Am. A* **19**(9), 1748–1754 (2002).
18. Y. L. Sheng and L. X. Shen, "Orthogonal Fourier-Mellin moments for invariant pattern recognition," *J. Opt. Soc. Am. A* **11**(6), 1748–1757 (1994).
19. H. Ren et al., "Multi-distorted invariant image recognition with radial-harmonic-Fourier moments," *J. Opt. Soc. Am. A* **20**(4), 631–637 (2003).
20. B. Xiao, J. F. Ma, and X. Wang, "Image analysis by Bessel-Fourier moments," *Pattern Recognit.* **43**(8), 2620–2629 (2010).
21. Z. Ping et al., "Generic orthogonal moments: Jacobi-Fourier moments for invariant image description," *Pattern Recognit.* **40**(4), 1245–1254 (2007).
22. M. Born and E. Wolf, *Principles of Optics*, Cambridge University, United Kingdom (1999).
23. T. V. Hoang and S. Tabbone, "Errata and comments on generic orthogonal moments: Jacobi-Fourier moments for invariant image description," *Pattern Recognit.* **46**(11), 3148–3155 (2007).
24. N. V. S. Sree Rathna Lakshmi and C. Manoharan, "An automated system for classification of microcalcification in mammogram based on Jacobi moments," *IJCTE* **3**(3), 431–434 (2011).
25. C. Camacho-Bello et al., "High precision and fast computation of Jacobi-Fourier moments for image description," *J. Opt. Soc. Am. A* **31**(1), 124–134 (2014).
26. C. Camacho-Bello, C. Toxqui-Quitl, and A. Padilla-Vivanco, "Generic orthogonal moments and applications," in *Moments and Moment Invariants*, G. Papakostas, Ed., pp. 175–204, Science Gate Publishing, Xhanti, Greece (2014).
27. G. Li-Qiang and Z. Ming, "Quaternion Fourier-Mellin moments for color images," *Pattern Recognit.* **44**(2), 187–195 (2011).
28. B. J. Chen et al., "Quaternion Zernike moments and their invariants for color image analysis and object recognition," *Signal Process.* **92**(2), 308–318 (2012).
29. Z. Shao et al., "Quaternion Bessel-Fourier moments and their invariants descriptors for object reconstruction and recognition," *Pattern Recognit.* **47**(2), 603–611 (2014).
30. E. G. Karakasis et al., "A unified methodology for computing accurate quaternion color moments and moment invariants," *IEEE Trans. Image Process.* **23**(2), 596–611 (2014).
31. S. X. Liao and M. Pawlak, "On the accuracy of Zernike moments for image analysis," *IEEE Trans. Pattern Anal. Mach. Intell.* **20**(12), 1358–1364 (1998).

32. Y. Xin, M. Pawlak, and S. Liao, "Accurate computation of Zernike moments in polar coordinates," *IEEE Trans. Image Process.* **16**(2), 581–587 (2007).

César Camacho-Bello received his BS degree in industrial engineering from the Autonomous University of Hidalgo State in 2006, his MS degree in optical computing from the Polytechnic University of Tulancingo in 2011, and his PhD in optics from the National Institute of Astrophysics, Optics, and Electronics in 2014. He is now a researcher in the Polytechnic University of Tulancingo, Mexico. His research interests include pattern recognition, biometric analysis, computer vision, and digital image processing.

Alfonso Padilla-Vivanco received his physics degree in 1994 from Puebla Autonomous University, Mexico, and his MS degree in 1995 and his PhD in 1999, both in optics, from the National Institute of Astrophysics, Optics, and Electronics. In 2000, he held a postdoctoral position in the Physics Department at the University of Santiago de Compostela, Spain. He is now a researcher at Polytechnic University of Tulancingo, Hidalgo, Mexico. His research interests include optical information processing, image analysis, and computer vision.

Carina Toxqui-Quitl is a researcher at the Polytechnic University of Tulancingo. She received her BS degree from the Autonomous University of Puebla, Mexico, in 2005 and her MS and PhD degrees in optics from the National Institute of Astrophysics, Optics, and Electronics in 2006 and 2010, respectively. Her current research areas include image moments, digital image processing, biomedical optics, and computer vision. She is also a member of SPIE.

José Javier Báez-Rojas received his MSc and PhD degrees from the Tokyo Institute of Technology, Japan, in 1991 and 1994, respectively. He is currently a researcher with the National Institute of Astrophysics, Optics, and Electronics in Mexico. His research interests include digital color, multispectral imagery, and digital image processing.